U. S. Naval Research Laboratory
Washington, DC 20375-5320

NRL/7160/FR--2021/6

On the Design, Modeling, and Fabrication of Hydrostatically Activated Negative Stiffness Inclusions

Stephanie G. Konarski

Acoustic Signal Processing and Systems Branch
Acoustics Division

June 21, 2021

REPORT DOCUMENTATION PAGE

Form Approved
OMB No. 0704-0188

1. REPORT DATE (DD-MM-YYYY)	2. REPORT TYPE	3. DATES COVERED (From – To)
21-06-2021	NRL Formal Report	19 FEB 2018 – 20 FEB 2020

4. TITLE AND SUBTITLE

On the Design, Modeling, and Fabrication of Hydrostatically Activated Negative Stiffness Inclusions

5a. CONTRACT NUMBER

5b. GRANT NUMBER

5c. PROGRAM ELEMENT NUMBER
NISE

6. AUTHOR(S)

Stephanie G. Konarski

5d. PROJECT NUMBER

5e. TASK NUMBER

5f. WORK UNIT NUMBER
N2N9

7. PERFORMING ORGANIZATION NAME(S) AND ADDRESS(ES)

U. S. Naval Research Laboratory
4555 Overlook Avenue, SW
Washington, DC 20375-5320

8. PERFORMING ORGANIZATION REPORT NUMBER

NRL/7160/FR--2021/6

9. SPONSORING / MONITORING AGENCY NAME(S) AND ADDRESS(ES)

U.S. Naval Research Laboratory
4555 Overlook Avenue, SW
Washington, DC 20375-5320

10. SPONSOR / MONITOR'S ACRONYM(S)
NRL-NISE

11. SPONSOR / MONITOR'S REPORT NUMBER(S)

12. DISTRIBUTION / AVAILABILITY STATEMENT
DISTRIBUTION STATEMENT A. Approved for public release: Distribution unlimited.

13. SUPPLEMENTARY NOTES
Karles Fellowship

14. ABSTRACT
Structures with non-convex potential energy functions that exploit mechanical instabilities possess local deformation states that correspond to negative stiffness. Only a dilute concentration of such inclusions offers the potential to create a composite material with simultaneously favorable acoustic and mechanical properties. This report iterates on aspects of design, numerical modeling, and fabrication of several example negative stiffness inclusions with mechanical instabilities. Additive manufacturing is utilized to fabricate the complex structures, which requires material characterization to ensure accurate numerical modeling. Different test inclusions are fabricated to inform the design of new structures and the associated numerical modeling to achieve the intended response. Numerical modeling of the nonlinear deformation of both inclusions and composite materials containing such inclusions within a hyperelastic host material are considered.

15. SUBJECT TERMS

16. SECURITY CLASSIFICATION OF:			17. LIMITATION OF ABSTRACT	18. NUMBER OF PAGES	19a. NAME OF RESPONSIBLE PERSON
a. REPORT	b. ABSTRACT	c. THIS PAGE			Stephanie G. Konarski
U	U	U	U/U	35	19b. TELEPHONE NUMBER *(Include area code)* 202-767-3524

Standard Form 298 (Rev. 8-98)
Prescribed by ANSI Std. Z39.18

This page intentionally left blank

CONTENTS

FIGURES

TABLES

ON THE DESIGN, MODELING, AND FABRICATION OF HYDROSTATICALLY ACTIVATED NEGATIVE STIFFNESS INCLUSIONS

1. INTRODUCTION

Composite materials containing distributed inclusions have long been studied to control the wave propagation through a material. Often, soft inclusions, e.g., air cavities, are embedded within a viscoelastic polymer [1]. However, this leads to a trade-off in tolerance to hydrostatic pressure loadings with optimal acoustic performance. It is thus of interest to design materials with simultaneously high stiffness and high damping. Inclusions with negative stiffness offer a promising path toward this goal. The usefulness of low-stiffness materials in energy dissipation applications has been long considered. However, it was not until work by Lakes and co-workers in the early 2000s that structural negative stiffness became a focus [2–8] and continues to be of increasing interest.

Early work on composite materials focused on negative stiffness phases achieved due to phase transformations, such as ferroelectric materials [3, 7, 9]. However, the buckling response associated with mechanical instabilities of a material or structure mimics that of the phase transformation, and likewise may be described by a fourth-order, nonconvex potential energy function [10, 11]. This negative stiffness is independent of frequency and therefore differs from the negative stiffness achieved through resonant effects typically studied with acoustic metamterials [12]. Additional efforts then focused on general mass-spring systems [8, 13, 14] and physical buckling structures such as thin beams [15–20]. Increased damping to achieve efficient energy dissipation of vibrations has been explored through single buckling elements [15, 16, 18], periodic lattices [19, 20], layered composites [21, 22], nonlinear energy sinks attached to linear structures [23, 24], and small-scale inclusions [17, 25–28]. Additionally, periodic lattices with mechanical instabilities may be employed to tune small-amplitude elastic wave propagation at large pre-stresses imposed on the structure to achieve nonreciprocal propagation [29, 30] and phononic switches with tunable band gaps [31, 32].

Of specific interest here is structural negative stiffness achieved through designed mechanical instabilities. One prominent design that can achieve structural negative stiffness is that of a clamped-clamped beam precurved into the first buckled mode [33]. The structure is deformed with an applied force at the center of the beam, such as the schematic shown in Fig. 1(a). Given appropriate geometric parameters, such as initial apex, beam length, and beam thickness, the resulting displacement due to an applied force becomes non-monotonic, such as shown in Fig. 1(b) with the blue curve. When the deformation state reaches a local extrema, i.e. point A, it will be unable to follow the natural trend of the force-displacement curve and instead will undergo snap-through deformation from point A to point B following the gray arrow. Snap-through, or snapping, corresponds to a large change in displacement due to a small change in force, stress, or pressure. Negative stiffness occurs for the strain states the mechanism missed by snapping to the next-highest stress state and represents an assistance to the applied load, rather than a resistance expected of a positive stiffness structure. The stiffness appears in Fig. 1(b) in orange. The deformed state of the beam in Fig. 1(a) at x_2 corresponds to a negative stiffness state that the mechanism is snapping through.

Manuscript approved June 21, 2021.

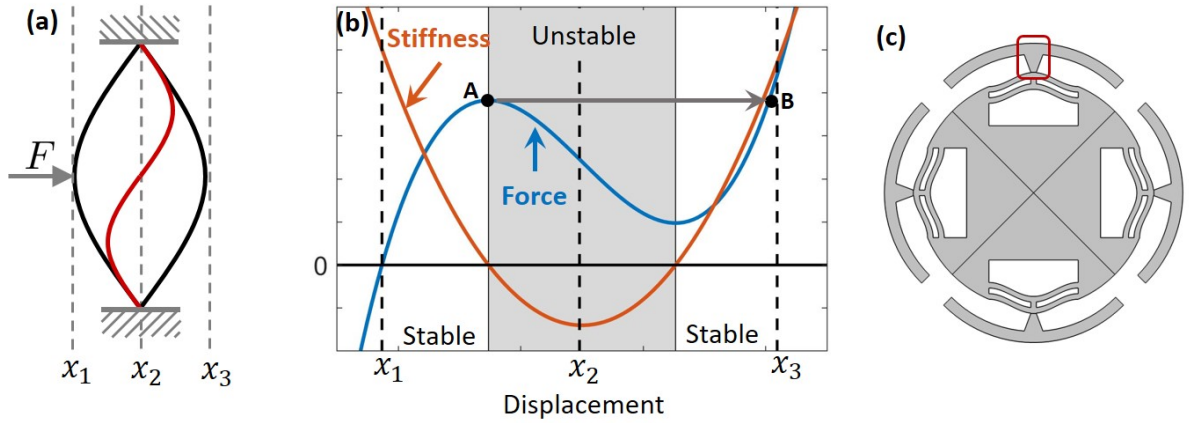

Fig. 1—Example of (a) a clamped-clamped beam at three deformation states, and (b) the resulting force (blue) and stiffness (orange) of the beam at three deformation states, and (c) a design configuration with double beam elements, with the pressure transformer highlighted in red

The clamped-clamped beam must be designed with appropriate combinations of geometric parameters, such as initial apex, beam length, and beam thickness, to achieve snap-through deformation characterized by structural negative stiffness. Use of double beam elements or thickness-modulated beam elements that constrain the second mode upon deformation results in a bistable response. An example inclusion design with double beam elements appears in Fig. 1(c). All previous considerations of this type of pre-curved beam design rely on deformation at the center of the beam [17–19, 26–28, 33]. This can be achieved by localizing a uniform load on the outer surface to the center of the beam through a pressure transformer, highlighted with red in Fig. 1(c).

In order to limit the overall deformation of the composite material and to localize the large displacements inherent with snap-through to the inclusion surface, only a dilute concentration of negative stiffness structures is embedded in the surrounding matrix material. This occurs when the magnitude of the inclusion stiffness is comparable to the surrounding matrix material. The associated high localized strains at the surface of only a few negative stiffness inclusions can result in enhanced energy dissipation for a viscoelastic solid [4, 17].

The main objective of this work is to explore the applicability of small-scale inclusions with negative stiffness that stems from structural instabilities to underwater acoustic applications. This first requires accurate characterization of the materials used to fabricate the inclusions, which are printed using additive manufacturing methods, and the host material in which the inclusion will be embedded. This is discussed in Section 2. Additionally, understanding the appropriate design and influence of the various geometric features is crucial in being able to fabricate a sample that will operate optimally. Different aspects of modeling such small-scale structures and the implications on fabrication are explored in Section 3. Ultimately, the behavior of interest corresponds to that of the inclusions within a host material. While the inclusions could be suspended in a fluid, it is of interest to properly capture the inclusions within an elastomer to achieve a favorable macroscale pressure tolerance. Aspects of the modeling composites that contain tailored, negative stiffness inclusions are considered in Section 4.

2. MATERIALS

Soft elastomers can exhibit geometric and material nonlinearity when subjected to large deformations, which can be difficult to quantify and model. There are many hyperelastic constitutive models, where strain energy density functions are introduced to derive stress-strain relationships under finite deformations. Section 2.1 introduces three hyperelastic models that will be utilized throughout this report: the nearly incompressible Neo-Hookean model, the nearly incompressible two-parameter Mooney-Rivlin model, and the Murnaghan model. Since these are phenomenological in nature, curve-fitting techniques are required to characterize real materials for use in modeling. The absence of well-defined material properties from either the manufactures of the material or in the academic literature for both soft elastomers in general or three-dimensional (3D) printed materials makes design of complex structures difficult. While continuing advancements in additive manufacturing offer the ability to fabricate intricate microstructures, exact material properties can depend on printing conditions and external environments. Section 2.2 provides some initial material characterization for 3D-printed rigid plastic materials, as well as soft elastomers that are both printed and cured in molds.

2.1 Hyperelastic Material Modeling

The strain energy density W for hyperelastic models is typically defined with invariants of the deformation gradient F_{ij}, the elastic right Cauchy-Green deformation tensor $C_{ij} = F_{ki}F_{kj}$, or the elastic Green-Lagrange strain tensor $E_{ij} = (C_{ij} - \delta_{ij})/2$. For the hyperelastic models of interest here, it is most convenient to derive the second Piola-Kirchhoff stress, $S_{ij} = \partial W/\partial E_{ij} = 2\partial W/\partial C_{ij}$. However, the Cauchy stress is utilized in comparing the uniaxial response with tensile testing data. Therefore,

$$\sigma_{ij} = J^{-1} S_{ik} C_{jk}, \tag{1}$$

where the Jacobian $J = \det \boldsymbol{F}$. Three materials models are considered throughout this report: nearly incompressible Neo-Hookean, nearly incompressible two-parameter Mooney-Rivlin, and Murnaghan. The Neo-Hookean and two-parameter Mooney-Rivlin models are functions of C_{ij}, while the Murnaghan model is expressed in terms of E_{ij}. All three models are common hyperelastic models employed by commercial finite element model software and the form of the strain energy density matches those in the software COMSOL 5.5 for ease of implementation when modeling such materials.

In general, the invariants assume the following functional form for any tensor A_{ij}:

$$\begin{aligned} I_{A1} &= A_{jj}, \\ I_{A2} &= \frac{1}{2}\left(I_{A1}^2 - A_{jk}A_{jk}\right), \\ I_{A3} &= \det\left(A_{ij}\right). \end{aligned} \tag{2}$$

Some measure of stress (either first or second Piola-Kirchhoff) then may defined from

$$\frac{\partial W}{\partial A_{ij}} = \frac{\partial W}{\partial I_{A1}}\delta_{ij} + \frac{\partial W}{\partial I_{A2}}\left(I_{A1}\delta_{ij} - A_{ji}\right) + \frac{\partial W}{\partial I_{A3}} I_{A3} A_{ji}^{-1}. \tag{3}$$

Here, A_{ij} will refer either to C_{ij} or E_{ij}.

For nearly incompressible materials, it is often more convenient to decompose the strain energy density into a volumetric component and an isochoric component, such that the total strain energy density is $W = W^{\text{iso}} + W^{\text{vol}}$. The volumetric components is defined as

$$\sigma_{ij}^{\text{vol}} = \frac{\partial W^{\text{vol}}}{\partial J}\delta_{ij}. \tag{4}$$

The nearly incompressible models of interest are defined in terms of the invariants for C_{ij}, which become

$$\begin{aligned} \bar{I}_{C1} &= J^{-2/3} I_{C1}, \\ \bar{I}_{C2} &= J^{-4/3} I_{C2}, \\ \bar{I}_{C3} &= J^{2}. \end{aligned} \tag{5}$$

Then, isochoric component of the Cauchy stress is

$$\begin{aligned} \sigma_{ij}^{iso} &= 2J^{-1}\frac{\partial W^{\text{iso}}}{\partial C_{ik}} C_{jk} \\ &= \frac{2}{3} J^{-5/3}\frac{\partial W}{\partial \bar{I}_{C1}}\left(3C_{ij} - I_{C1}\delta_{ij}\right) + \frac{2}{3} J^{-7/3}\frac{\partial W}{\partial \bar{I}_{C2}}\left(3I_{C1}C_{ij} - 3C_{ik}C_{jk} - 2I_{C2}\delta_{ij}\right). \end{aligned} \tag{6}$$

When comparing to unixaxial tensile testing data, the only non zero stress component is σ_{11}. In this case, let $C_{11} = \lambda^2$, $C_{22} = C_{33} = \lambda^{-1}J$, and the off-diagonal terms of C_{ij} equal zero. The principal stretch λ defines the normalized change in displacement.

2.1.1 Nearly incompressible Neo-Hookean

The strain energy density for the nearly incompressible Neo-Hookean model is defined in terms of the bulk modulus K, the shear modulus G, and the nearly incompressible invariants of the C_{ij} tensor as

$$W = \frac{1}{2}G\left(\bar{I}_{C1} - 3\right) + \frac{1}{2}K\left(J-1\right)^2. \tag{7}$$

The Cauchy stress is then

$$\sigma_{ij} = \frac{1}{3}J^{-5/3}G\left(3C_{ij} - I_{C1}\delta_{ij}\right) + K\left(J-1\right)\delta_{ij} \tag{8}$$

such that under uniaxial tension,

$$\begin{aligned} \sigma_{11} &= \frac{2}{3}J^{-2/3}\lambda^{-1}\left(J^{-1}\lambda^3 - 1\right)G + K\left(J-1\right) \\ &= J^{-2/3}\lambda^{-1}\left(J^{-1}\lambda^3 - 1\right)G. \end{aligned} \tag{9}$$

In the limit of incompressibility, $J \to 1$ and σ_{11} is only a function of principal stretch λ in the 11-direction and coefficients C_{10} and C_{01}.

2.1.2 Nearly incompressible two-parameter Mooney Rivlin

Mooney-Rivlin materials are described by a class of strain energy functions at different orders of the three invariants, which is sometimes called the polynomial hyperelastic material. The two-parameter version of the strain energy density is the first-order approximation with coefficients C_{10} and C_{01}, which define the shear modulus $G = 2\left(C_{10} + C_{01}\right)$, the bulk modulus K, and the nearly incompressible invariants of the C_{ij} tensor, where

$$W = C_{10}\left(\bar{I}_{C1} - 3\right) + C_{01}\left(\bar{I}_{C2} - 3\right) + \frac{1}{2}K\left(J-1\right)^2. \tag{10}$$

The Cauchy stress is then

$$\sigma_{ij} = \frac{2}{3}C_{10}J^{-5/3}\left(3C_{ij} - I_{C1}\delta_{ij}\right) + \frac{2}{3}C_{01}J^{-7/3}\left(3I_{C1}C_{ij} - 3C_{ik}C_{jk} - 2I_{C2}\delta_{ij}\right) + K\left(J-1\right)\delta_{ij} \tag{11}$$

such that under uniaxial tension,

$$\begin{aligned}\sigma_{11} &= \frac{4}{3}J^{-1/3}\lambda^{-2}\left(J^{-1}\lambda^3 - 1\right)\left(J^{-1/3}\lambda C_{10} + C_{01}\right) + K\left(J-1\right), \\ &= 2J^{-1/3}\lambda^{-1}\left(J^{-1}\lambda^3 - 1\right)\left(J^{-1/3}\lambda C_{10} + C_{01}\right).\end{aligned} \tag{12}$$

In the limit of incompressibility, $J \to 1$ and σ_{11} is only a function of principal stretch λ in the 11-direction and shear modulus G.

2.1.3 Murnaghan

The strain energy density for the Murnaghan model is defined in terms of bulk modulus K, shear modulus G, third-order elastic constants ℓ, m, and n, and invariants of the strain tensor E_{ij} as

$$W = \frac{1}{2}\left(K + \frac{4}{3}G\right)I_{E1}^2 - 2GI_{E2} + \frac{1}{3}\left(\ell + 2m\right)I_{E1}^3 - 2mI_{E1}I_{E2} + nI_{E3}. \tag{13}$$

The Cauchy stress tensor is

$$\begin{aligned}\sigma_{ij} = 2J^{-1}\Bigg\{\left[\left(K - \frac{2}{3}G\right)I_{E1} + \ell I_{E1}^2 - 2mI_{E2}\right]\left(E_{ij} + \delta_{ij}\right) \\ +2\left(G + mI_{E1}\right)\left(E_{ik}E_{jk} + E_{ij}\right) + nI_{E3}\left(E_{ik}^{-1} + \delta_{ij}\right)\Bigg\}\end{aligned} \tag{14}$$

such that the uniaxial stress in the 11 direction is

$$\sigma_{11} = 2J^{-1}\left(1 + E_{11}\right)\left[\left(K - \frac{2}{3}G\right)I_{E1} + 2GE_{11} + \ell I_{E1}^2 + 2m\left(I_{E1}E_{11} - I_{E2}\right) + nE_{22}^2\right]. \tag{15}$$

In the limit of incompressibility, $J \to 1$ and orders of I_{E1} may be neglected [34]. Then, σ_{11} is only a function strain components E_{11}, E_{22}, and I_{E2}, and moduli G, m, and n.

2.2 Material Characterization

One prominent method of characterizations is uniaxial tensile testing of "dogbone" specimens. The shape of the test samples is specified in the ASTM Standard D638-02: Standard test method of tensile properties of plastics [35] depending on the type of plastic. For a specimen in tension, a loading force F inducing a change in length $L - L_0$ from the initial length L_0 and a change in width from the initial width w_0. The (nominal) engineering stress is then defined by $\sigma_{lx} = F/A_0$, where $A_0 = L_0 w_0$ is the initial cross-section. Note that change in length corresponds to deformation in the x-direction and change in width corresponds to the change in the y-direction. The (nominal) engineering strains in the x- and y-directions are $\varepsilon_{lx} = L/L_0 - 1$ and $\varepsilon_{ly} = w/w_0 - 1$, respectively. In the linear regimes, the Young's modulus and Poisson's ratio are defined as

$$Y = \frac{\sigma_{lx}}{\varepsilon_{lx}}, \tag{16}$$

$$\nu = -\frac{\varepsilon_{ly}}{\varepsilon_{lx}}. \tag{17}$$

Tensile testing was performed on an ADMET eXpert 2611 compression system. The results are now described for the rigid plastics and soft elastomers. All values are obtained by averaging 3 or 4 samples, depending on the material. The moduli reported below are of the form $\bar{x} \pm x_e$, where $\bar{x}$ is the average value and x_e is the margin of error. The margin of error depends on the number of samples N, the standard deviation of the data s_x, and a constant α based on the error confidence interval and the distribution type, such that $x_e = \alpha s_x/\sqrt{N}$ [36]. For a small number of averages, nominally fewer than 30, the t-distribution is recommended because it accounts for an increased uncertainty associated with few samples. As the number of samples increases, the t-distribution approaches that of the normal (z-) distribution. For a 95% confidence interval with a t-distribution, $\alpha = 4.303$ for 3 samples and $\alpha = 3.182$ for 4 samples.

The linear moduli of three rigid plastics, all fabricated with Stratasys Polyjet Printers (J750 and Connex500), are measured here: a simulated ABS plastic DigitalABS, and two simulated polypropylene materials, Rigur and DurusWhite. The samples were fabricated with the dimensions defined for the Type I specimen in ASTM 638-02 [35]. Axial and transverse strain gauges (Epsilon Technology Corp.) were used to obtain the displacement of the gauge section in the x- and y- directions. Without the transverse strain gauge, the Poisson's ratio cannot be calculated. The average value and error margin based on the 95% confidence interval of a t-distribution for Young's modulus in GPa and Poissons' ratio, as well as the range of Young's moduli values provided by Stratasys, appear in Table 1. Stratasys does not provide values for Poisson's ratio, though plastics typically posses values near $0.35 - 0.4$. Although the average measured values are on the

Table 1—Linear Elastic Properties for Rigid Plastic Samples

	Measured		**Stratasys**
Material	**Young's Modulus (GPa)**	**Poisson's Ratio**	**Young's Modulus (GPa)**
DigitialABS	2.65 ± 0.6	0.37 ± 0.03	2.6 – 3.0
Rigur	1.65 ± 0.03	0.34 ± 0.04	1.7 – 2.1
DurusWhite	1.0 ± 0.27	0.42 ± 0.07	1.0 – 1.2

lower end of the ranges provided by Stratasys, there is still reasonable agreement. Increasing the number of samples will provide more accurate data.

Several candidate soft elastomers are considered that could be 3D printed materials: two Stratasys polyjet materials named TangoPlus and Agilus30, and a thermoplastic polyurethane called NinjaFlex printed using the fused deposition modeling (FDM) technique. Other materials were created using the more traditional method of casting in molds: Momentive RTV615, a polydimethylsiloxane (PDMS) material, and two polyurethanes, VytaFlex and ReoFlex, from Smooth-On. All samples were fabricated following the dimensions for Type IV from the ASTM Standard D638-02, which is identical to the dimensions specified in the ASTM Standard: Standard test for vulcanized rubbers and thermoplastic elastomers - Tension [37]. Tensile testing with the ADMET was performed, but the extensometers could not be used because the materials were too soft. Therefore, measurements of the Poisson's ratio were not possible at this time. Instead, it is assumed that the materials are nearly incompressible, with ν near 0.49 - 0.5. The average Young's modulus (Y) in MPa based on the linear elastic response for four samples of each soft elastomer is shown in Table 2 with the margin of error based on the 95% confidence interval for the t-distribution. Note that the material TangoPlus is denoted as Tango+. The manufacturers of these materials do not provide estimates for Young's modulus. The approximate shear modulus, based on assuming that $\mu = Y/3$ when $\nu = 0.5$, is calculated and appears in the table for reference. To verify the Poisson's ratio, an alternative method, such as video imagining, would be required.

To consider the nonlinear deformation, the "curve fit" function within Python's SciPy Optimize subpackage [38] was employed to fit the nonlinear data to the incompressible uniaxial Cauchy stress of the Neo-Hookean, two-parameter Mooney-Rivlin, and Murnaghan models. Under this assumption, $J = 1$ for the Neo-Hookean model in Eq. (9), the Mooney Rivlin model in Eq. (12), and the Murnaghan model with all orders of I_{E1} neglected [34] in Eq. (15). The values of the relevant elastic moduli obtained from the curve fitting appear in Table 2, where the margin of error for the curve fit coefficients represents a 95% confidence interval for the normal distribution, with $\alpha = 1.96$. Although the incompressible assumptions correspond to the case of $K \to \infty$, the moduli in Table 2 could be used in conjunction with a bulk modulus two or more orders of magnitude larger than the shear modulus for the purposes of modeling. The coefficient of determination R^2 quantifies the "goodness of fit" and is defined by [36]

$$R^2 = 1 - \frac{\sum (y_i - f_i)^2}{\sum (y_i - \bar{y})^2}, \tag{18}$$

where $\bar{y}$ is the mean of the observed data, y_i is each data point, and f_i is the function evaluated with the moduli obtained from the curve fit at each value. The coefficient of determination provides a metric of quantifying the variance in the predicted stress based on the moduli obtained from the curve fitting relative to the data. Values of R^2 closer to 1 correspond to less variance in the predicted solution.

Table 2—Hyperelastic Properties for Soft Elastomeric Samples

		Agilus	**Tango+**	**NinjaFlex**	**VytaFlex**	**ReoFlex**	**PDMS**
Linear	Y (MPa)	0.86	0.84	18.46	4.94	3.38	2.03
		±0.13	±0.16	±0.56	±0.52	±0.12	±0.66
	G (MPa)	0.29	0.28	6.21	1.65	1.13	0.68
Neo-Hookean	G (MPa)	0.22	0.17	3.61	1.29	0.86	0.57
		± 0.001	±0.001	±0.05	±0.01	±0.006	±0.003
	R^2	0.9775	0.9862	0.8792	0.9620	0.9555	0.9831
2–Parameter Mooney–Rivlin	C_{10} (MPa)	-0.19	-0.10	-3.39	-1.02	-0.59	-0.33
		± 0.007	±0.004	± 0.069	±0.007	±0.07	±0.006
	C_{01} (MPa)	0.32	0.20	6.17	1.89	1.6	0.68
		± 0.008	± 0.004	±0.089	± 0.009	±0.008	±0.008
	G (MPa)	0.27	0.21	5.57	1.73	1.14	0.7
	R^2	0.9964	0.9979	0.9938	0.9997	0.9994	0.9992
Murnaghan	G (MPa)	0.48	0.34	9.79	2.70	1.83	1.14
		± 0.004	±0.004	±0.055	±0.006	±0.002	±0.003
	m (MPa)	2.23	0.38	1.43	-1.38	-0.55	0.62
		± 0.167	±0.094	±0.416	±0.088	±0.029	±0.58
	n (MPa)	-36.53	-14.45	-379.96	-79.72	-56.78	-43.53
		± 1.645	±1.032	±6.881	±1.114	±0.405	±0.687
	R^2	0.9988	0.9986	0.9992	0.9999	0.9999	0.9999

The average measured uniaxial stress-strain data from the ADMET (black, solid line) is compared directly to the calculated stress for the Neo-Hookean model (dotted, blue line), the two-parameter Mooney-Rivlin model (dot-dashed, orange line), and the Murnaghan model (dashed, green line) are shown in Fig. 2 for (a) Agilus, (b) TangoPlus, (c) NinjaFlex, (d) VytaFlex, (e) ReoFlex, and (f) PDMS. The gray corresponds to the 95% confidence interval for the t-distribution for the mean of the three dogbone samples. In all cases, the Neo-Hookean model, with only one free parameter, is the worst predictor of the uniaxial deformation, whereas the Murnaghan model appears to be the best. For the VytaFlex and RytaFlex, the two-parameter Mooney-Rivlin parameter also strongly captures the measured data, and is very similar to the Murnaghan model.

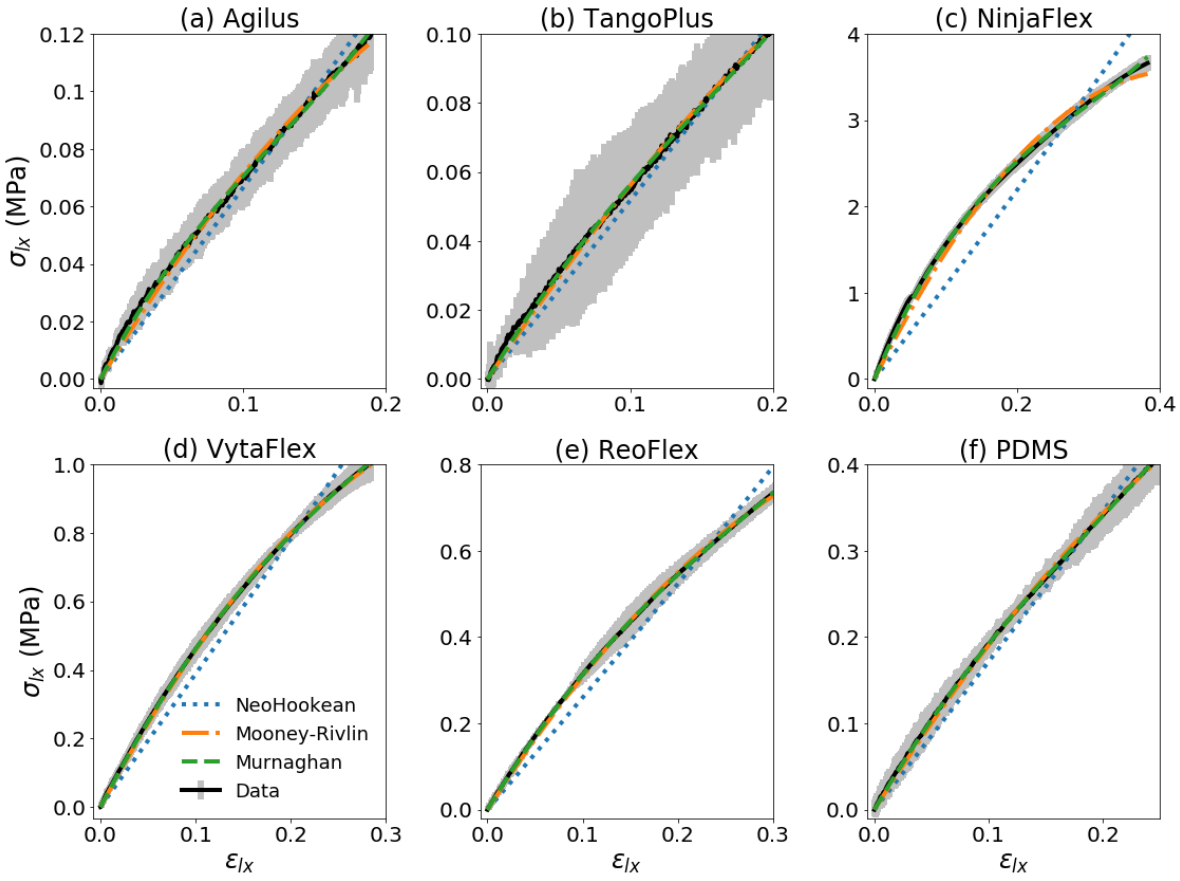

Fig. 2—Comparison of uniaxial stress σ_{lx} versus strain ε_{lx} for the data obtained with the ADMET (black) with error bars defined by the 95% confidence interval for the t-distribution (gray) with the fitted moduli for the Neo-Hookean (dotted blue), two-parameter Mooney-Rivlin, (dot-dashed orange), and Murnaghan (dashed green) models for (a) Agilus, (b) TangoPlus, (c) NinjaFlex, (d) VytaFlex, (e) ReoFlex, and (f) PDMS

The error varies substantially between materials. The widths of the error bounds above and below the data curve from smallest to largest are NinjaFlex, VytaFlex, ReoFlex, PDMS, Agilus, and TangoPlus. The trend for amount of error is the same as for the average Young's modulus in the linear regime, as shown in Table 2. Stiffer materials appear to exhibit more accurate curve fitting due to less variance between the measured stress strain for different dogbone samples. For the case of the TangoPlus in Fig. 2(b), the Neo-Hookean model does not follow the trend of the average data, but still fits within the error bounds, which makes it more difficult to discern the appropriate fitting parameters. If more dogbone samples were measured, the error in the average data should go down. Therefore, for soft materials, it is important to test a sufficient number of samples to provide accurate results. Additionally, recent studies have indicated that relaxation is important for TangoPlus and may affect the elastic properties if not accounted for properly [39]. The larger variance also may stem from print-to-print differences.

Furthermore, it is well established that use of only uniaxial data to obtain hyperelastic material moduli is insufficient to accurately model the same material under other loading conditions [40]. While the present analysis provides initial estimates of appropriate material models and approximate moduli, future work is certainly needed to better understand the nonlinear and viscoelastic material properties of such soft

elastomers, especially those that are 3D printed. Additionally, Stratasys Polyjet printers offer the ability to print “digital materials" that are gradient combinations of the hard plastics (DigitalABS, Durus, Rigur) and soft elastomers (TangoPlus, Agilus). Characterizing these digital materials will further open the design space of the possible acoustic and elastic response that will be explored in the remainder of this report.

3. INCLUSION DESIGN WITH STRUCTURAL NEGATIVE STIFFNESS

Several designs are considered in the following sections with pre-buckled structures that exhibit structural negative stiffness. First, a brief description of the modeling appears in Section 3.1. Simple one-dimensional (1D) test beams fabricated based on previously considered designs with a pressure transformer in the center [17, 26, 27, 33] provide preliminary insight into fabrication of structures, as discussed in Section 3.2. Based on the initial fabrication efforts, new designs were considered that include both pre-curved beams without a pressure transformer in Section 3.3 and pre-curved plates without a pressure transformer in Section 3.4. Both modeling and fabrication efforts are discussed in Sections 3.3–3.4.

3.1 Analytic Modeling

Structures with negative stiffness are described by a non-convex potential energy function W. It is assumed that the negative stiffness inclusions can be approximated as a sphere undergoing volumetric deformation. Let the normalized displacement ξ be defined as

$$\xi = \frac{R - R_0}{R_0}, \tag{19}$$

where R is the current, or instantaneous, radius and R_0 is the global equilibrium radius. For purely radial deformations, the only non zero component of the displacement vector is the radial component, where

$$u_r = \xi r \tag{20}$$

and r is the radial coordinate in the undeformed (Lagrangian) coordinate. The deformation gradient and Green-Lagrange strain tensors are then

$$F_{ij} = (1 + \xi)\, \delta_{ij}, \tag{21}$$

$$E_{ij} = \frac{1}{2}\left(F_{jk}F_{ik} - \delta_{ij}\right) = \left(\xi + \frac{1}{2}\xi^2\right)\delta_{ij} \equiv E\delta_{ij}. \tag{22}$$

Therefore, ξ represents the infinitesimal strain limit of the strain field under finite deformations. Since only radial deformation is assumed, the only non zero components of the stress tensor are also on the diagonal. Therefore, the second Piola-Kirchhoff stress may be defined as

$$S_{ij} = \frac{\partial W}{\partial E_{ij}} \equiv S\delta_{ij}. \tag{23}$$

It is also convenient to define the hydrostatic pressure, which is equal to $-\sigma_{kk}/3$, where σ_{kk} is the Cauchy stress tensor. The Cauchy stress is related to the second Piola-Kirchhoff stress in Eq. (1). The hydrostatic pressure is then

$$P = -\frac{1}{3}\left(1+\xi\right)^{-3}\left(1+\xi\right)\delta_{jk}S\delta_{kl}\left(1+\xi\right)\delta_{jl} = -\left(1+\xi\right)^{-1}S. \tag{24}$$

In linear elasticity, the stiffness tensor is defined as the derivative of stress with respect to strain. For nonlinear materials, there are several formulations of stress and strain to choose from. Here, the Lagrangian stiffness tensor is defined as

$$L_{ijkl} = \frac{\partial S_{ij}}{\partial E_{kl}} \equiv \frac{\partial S}{\partial E}\delta_{ij}\delta_{kl} \equiv \kappa\delta_{ij}\delta_{kl}. \tag{25}$$

The stiffness κ varies as a function of deformation and could become negative for some strain states. The analytic method of modeling has been implemented previously [26, 27, 41] for use on pre-curved beams with a pressure transformer that localizes the displacement to the center of the beams. It is now employed here for the alternative designs discussed in Sections 3.3–3.4.

3.2 Fabrication of Test Beams

Initial samples are 1D test beams with pressure transformers fabricated out of the three candidate plastics – Digital ABS, Rigur, and DurusWhite – to assess their applicability to a small-scale inclusion design. In addition to the difference in material properties, different geometric features were explored, including the length of the beam, the thickness of the beam, and the initial apex of the pre-curved shape. While all elements include only a single beam, some have a uniform thickness, while others are variable in thickness. Figures 3(a), 3(b), and 3(c) show a selection of the different test beams printed out of Rigur, DurusWhite, and DigitalABS, respectively. The longest samples posses a beam length of 30 mm, while the shorter beams are 20 mm in length. The outer walls connected to the left and right of the beam intend to create a clamped-clamped boundary condition. The length of each outer wall is one-quarter of the length of the beam, such that the longer beam elements have a total length of 45 mm and shorter beam structures have a total length of 30 mm. The out-of-plane extruded width of the beam design was 5 mm, but the as-fabricated values ranged from 4.9 mm to 5.15 mm.

Structures were deformed by hand. The use of a pressure transformer allows for the elements to be deformed at the center of the beams regardless of the applied load. Several key insights were learned from deforming these simple structures by hand. First, many elements fractured due to the high stress concentrations that caused failure of the material. The broken components occur either at the center, where the stress concentrator connects to the beam, or on the side where the beam connects to the outer support structure. "Softer" beams may be achieved through a smaller initial apex or a longer beam, assuming all other features are equal. Unsurprisingly, the softer beams were less likely to fracture because they require a lower pressure activation and therefore, introduce less stress in the material. However, softer beams correspond to less or no negative stiffness. Although structures fabricated from all three materials broke, there was more success with DurusWhite material than with DigitalABS and Rigur. This is because the DurusWhite material is characterized by a higher elongation at break, indicating that it can deform more before failure. The overall stiffness of the beam is determined through a combination of geometric and physical properties, all of which must be accounted for to ensure the structures do not fracture.

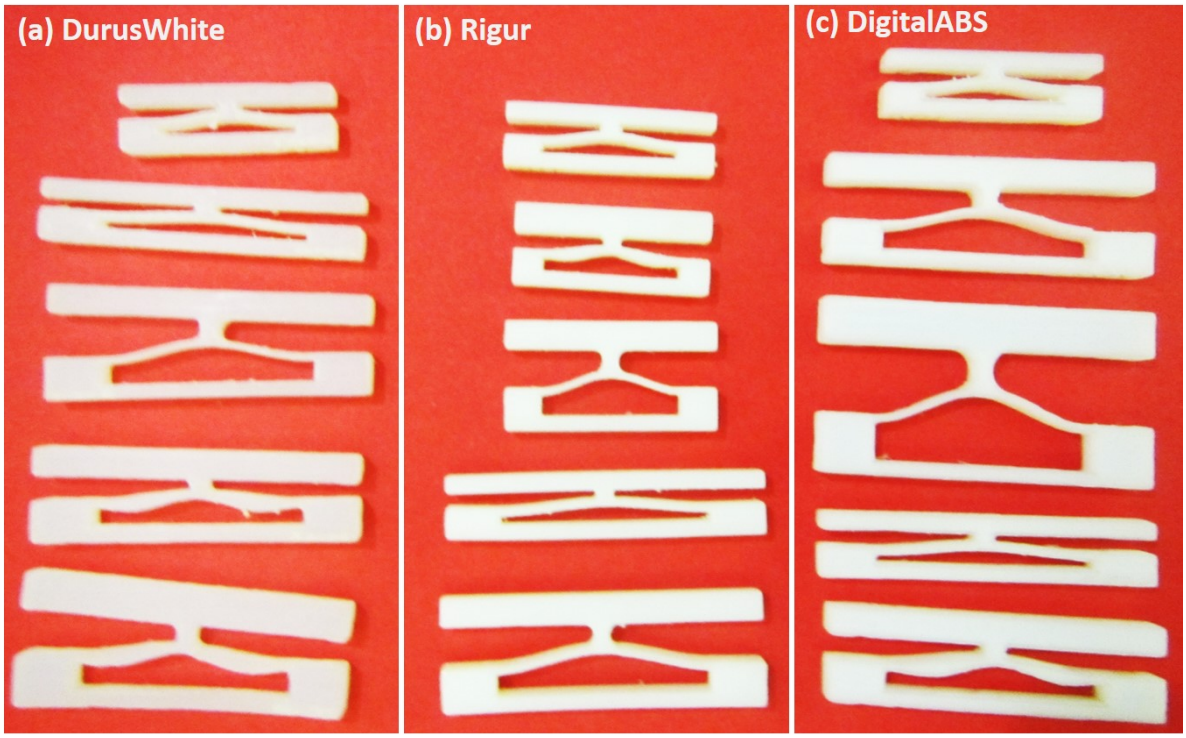

Fig. 3—Example 1D test pieces with different geometric properties of the pre-curved beams were printed out of (a) Rigur, (b) DurusWhite, and (c) DigitalABS

Additionally, for many of the test beams, upon deforming, the outer structure flexes outward instead of acting as an approximately rigid boundary. This outer boundary is important to ensure the negative stiffness response is achieved and must be designed carefully to ensure it constrains the beams appropriately. The boundary conditions utilized in numerical simulation also must be considered carefully. This qualitative analysis of the beam deformation indicates that real boundary conditions are often not identical to the idealized settings employed during modeling.

The next set of test structures are actual inclusion designs. A cylindrical design is much easier to fabricate than a spherical one. Therefore, the initial test inclusions are cylinders with beam elements on the top and bottom. The first set of elements were fabricated in two halves, as shown in Fig. 4(a), and then glued together with epoxy to create a single piece, as shown in Fig. 4(b). However, a new, soluble support material by Stratasys enables the inclusion to be fabricated in one piece, then soaked in a solution of sodium hydroxide to remove the internal support. Example inclusions fabricated as one piece appear in Fig. 4(c). Although the soluble support material simplifies fabrication, it limits the previously studied plastics to the DigitalABS material, which appears to be less favorable than the DurusWhite.

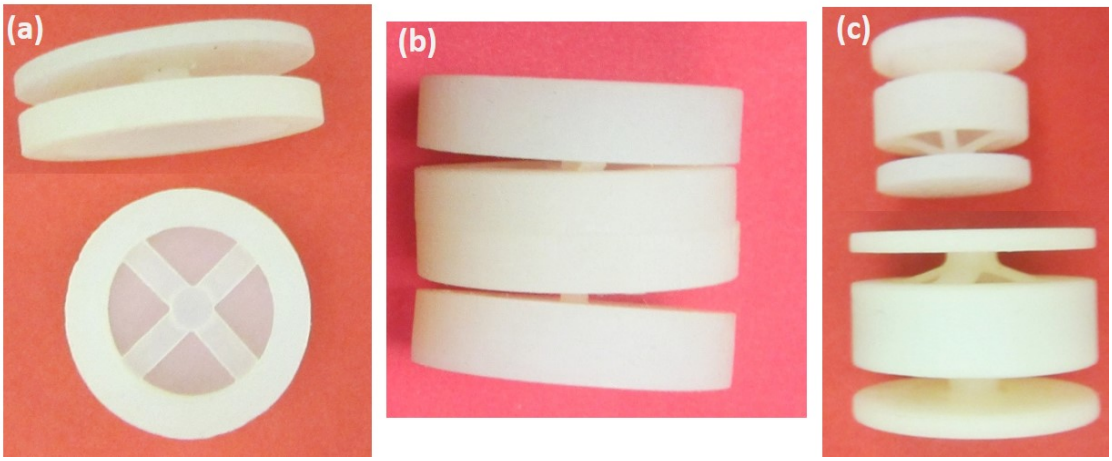

Fig. 4—Example test cylindrical inclusions with pre-curved beam elements printed either (a) as two separate halves and (b) then assembled as one inclusions with epoxy, or (c) as one piece with soluble support material

The cylindrical inclusions were deformed using the ADMET with smooth plattens attached to the top and bottom of the compression system. The bottom platten is fixed and the top platten compresses the cylindrical inclusion from the top. One resulting force-displacement curve obtained is shown in Fig. 5 for both loading and unloading of the structure. As the platten compresses the inclusion, it deforms the top beam elements nonlinearly until it reaches a point of instability. This is denoted by the black, dashed line at a displacement of 1.6 mm. The top beams then deform into the region characterized by negative stiffness, which is labeled as "NS Region of top beam" in Fig. 5. When the inclusion reaches a local minimum, the imposed displacement begins loading the bottom beam elements until it once again reaches a point of instability, denoted by the black, dashed line at 4.2 mm. The bottom beams then deform into another negative stiffness region denoted by "NS Region of bottom beam". Further loading beyond the two NS regions results in a strain-hardening effect.

Upon unloading, the system reaches similar points of instability that result in the beam snapping back to its original configuration. This loading is consistent with measurements obtained for periodic lattice arrangements of negative stiffness structures [19]. The force-displacement response under uniaxial compression differs from that of uniform hydrostatic loading on both the top and the bottom. In the latter case, the top and bottom beams would deform into the negative stiffness region at the same time. However, the non-monotonic nature of the force-displacement curve indicates that the instabilities exist, resulting in negative stiffness, and that the loading and unloading paths are different.

Unfortunately, the chosen design for the test cylinders also resulted in broken components due to high stress concentrations where the beam connects to another part of the structure, as was observed for the single test beams. In Fig. 5, there is only one instability point upon unloading because the beam structure broke before reaching the original undeformed configuration. These two preliminary fabrication studies on both the single beam elements and cylindrical inclusions motivate design of structures that eliminates the fragile pressure transformer that may break due to high stress concentrations. Design and modeling of such elements are considered in the following sections.

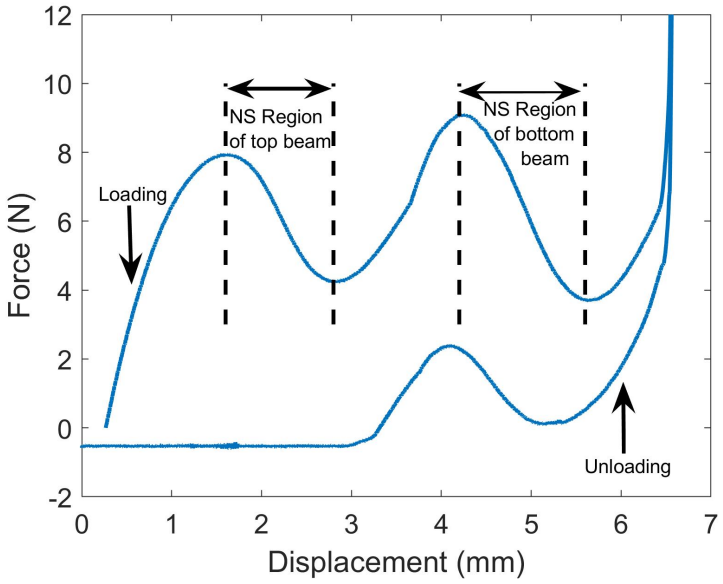

Fig. 5—Measured force-displacement curve from the ADMET for loading and unloading of one example cylindrical inclusion

3.3 Uniform Loading of Pre-curved Beams

The shape of the pre-curved beam element corresponds to flat, clamped-clamped beam buckled into its first mode. The height of the beam H as a function of space x is defined from [33] as

$$H(x) = \frac{h}{2}\left[1 - \cos\left(\frac{2\pi x}{L}\right)\right], \tag{26}$$

where h is the initial apex of the beam and L is the width of the beam. While it is possible to achieve a non-monotonic force-displacement response for a single beam element, bistability is achieved through constraining the second deformation mode of the beam. Qiu et al. demonstrated that bistability can be achieved through either a double beam element with two single beams connected at their geometric center or a single beam with non-uniform thickness defined by [33]

$$T(x) = t + \frac{1}{2}\delta t\left[1 - \cos\left(\frac{4\pi x}{L}\right)\right], \tag{27}$$

where the thinnest component has width t and the thickest component has width $t + \delta t$.

One possible solution is to apply a uniform force over the entire outer surface of the beam rather than to utilize a pressure transformer to mimic a point load at the center of the beam. The following analysis with uniform pressure loading is for several beam designs: a single beam element, a double beam element, and a thickness-modulated beam element. The geometric features for the single beam element shown in Fig. 6(a) are $t = 1$ mm, $h = 2$ mm, $L = 20$ mm, and a beam width of 2 mm. The double beam element shown in Fig. 6(b) includes two beams identical to that of the single beam element, spaced 1 mm apart. The

thickness-modulated beam is defined by the change in thickness $T(x)$ from Eq. (27) with $\delta t = 1$ mm and all other geometric features the same as the single beam, as shown in Fig. 6(c). All three cases are modeled in 3D for one-eighth of the structure due to symmetries with DigitalABS material properties from Table 1.

Monotonic loading parameters are required to deform structures using COMSOL. For materials exhibiting negative stiffness, a prescribed displacement is almost always monotonic, whereas a boundary load is not. However, by choosing a monotonic loading parameter, such as the displacement at a point that displays monotonic deformation, boundary loads may be applied (using "Global Equations" in COMSOL). For this inclusion design, the center point of the beam d_{center}, which is the outermost beam for the double beam element, will undergo monotonic displacement. Therefore, the deformation is solved for with a stationary study in COMSOL with geometric nonlinearity for a uniform pressure boundary load as a function of the center point displacement. Since all three inclusions are identical in initial apex and overall radius of the inclusion, d_{center} is identical for all three cases.

The corresponding deformation in the center cut plane appears in Figs. 6(d)–(l) at $d_{\text{center}} = 0$ mm in subplots 6(d)–(f), $d_{\text{center}} = 3.1$ mm in subplots 6(g)–(i), and $d_{\text{center}} = 5.7$ mm in subplots 6(j)–(l). The magnitude represents the von Mises stress. Although there is no deformation in Figs. 6(d)–(f), the figures clearly depict the beam design for a single beam element in Fig. 6(d), a double beam element with two beams connected only at the center in Fig. 6(e), and a single beam element with varying thickness in Fig. 6(f). When the inclusions are deformed to a state that would fall within the negative stiffness regime, e.g., configuration shown in Figs. 6(g)–(i) for $d_{\text{center}} = 3.1$ mm, the beams not only deform toward the center, but also exhibits increased stress at both the edge and center of the beam. The von Mises stress magnitude is further increased as the beams are displaced to $d_{\text{center}} = 5.7$ mm, especially at the edges and in the center, as shown in Fig. 6(j–l). The von Mises stress is an important indicator of whether the chosen material may fracture, causing the beam elements to break.

Also of note is the shape of the beam elements upon reaching the final state. The element with only one single beam in Fig. 6(j) appears to be the inverse of its initial state, which is not true for designs with the double beam in Fig. 6(k) or the variable-thickness in Fig. 6(l). For the double-beam element, the outermost beam undergoes uniform pressure loading, whereas the innermost beam is subjected to a load at its center point. This causes the spacing between the two beams to become non-uniform along the beams' length. For the variable-thickness beam, the center of the beam is more flat at $d_{\text{center}} = 5.7$ mm than at $d_{\text{center}} = 0$ mm because the thicker parts of the beam cannot undergo the same displacement as the thinner regions.

The strain percent as defined in Eq. (22), applied boundary pressure, and incremental stiffness as defined from Eq. (25), are shown in Fig. 7(a), (b), and (c), respectively, as a function of d_{center}. The gray dot-dashed line represents $d_{\text{center}} = 3.1$ mm, whereas the two endpoints represent $d_{\text{center}} = 0$ mm and $d_{\text{center}} = 5.7$ mm. There are minor differences in the strain as the beams are displaced, as evident in Fig. 7(a). All three inclusion designs have the same initial volume when accounting for the air that exists within the internal cavity. Therefore, the design of the beams minimally alters the change in volume with deformation, assuming that the initial volumes are the same or very similar.

Conversely, there are significant differences in the magnitude of the pressure loading as a function of displacement shown in Fig. 7(b). The single-beam element requires the lowest pressure to undergo the prescribed displacement, whereas the double-beam element requires the most. This trend is anticipated, since the increased mass associated with the second beam requires a larger force under the same displacement rate. The more interesting feature is the differences in slope, which represents the incremental stiffness

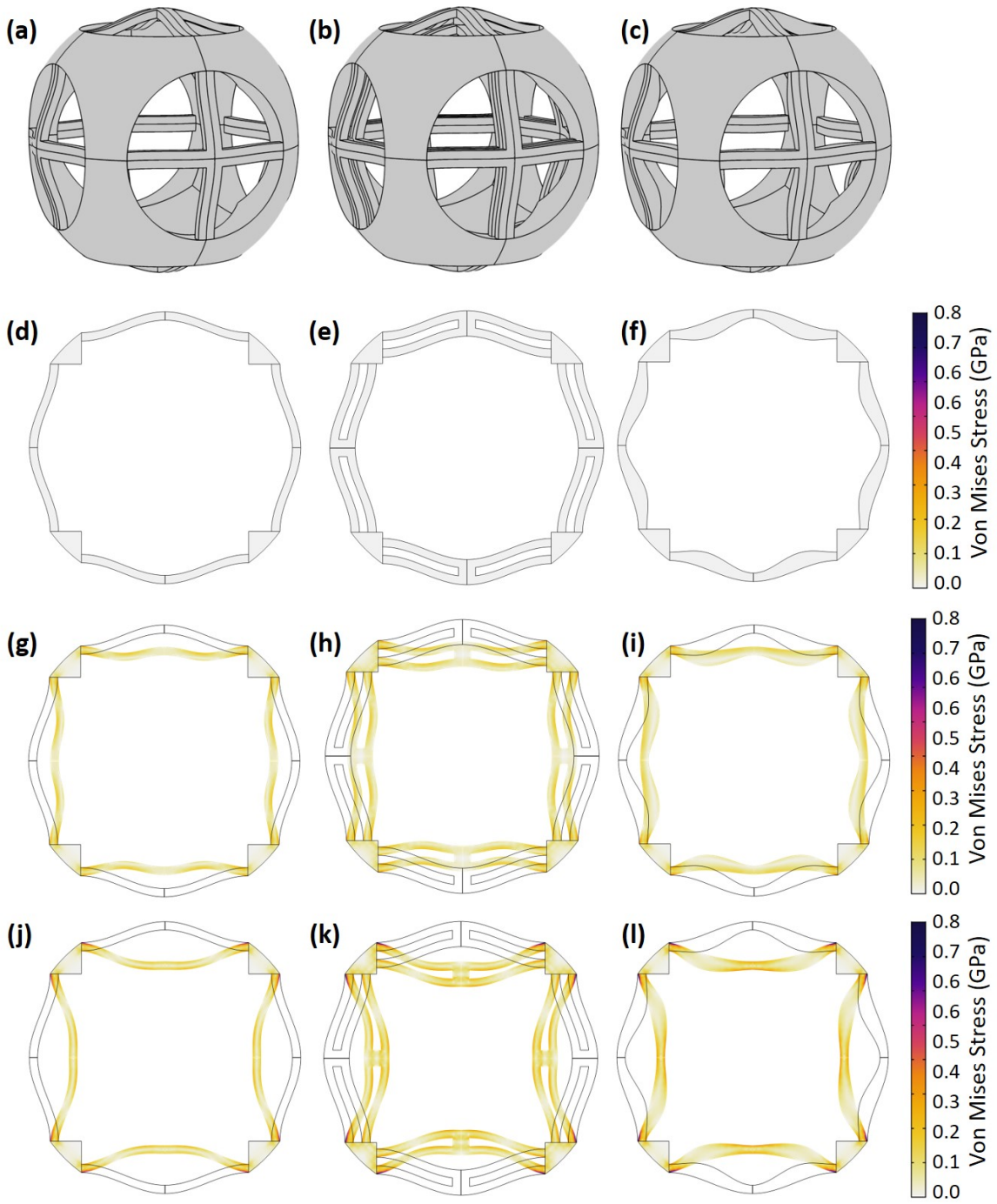

Fig. 6—3D inclusion spherical element for pre-curved (a) single, uniform beam, (b) double uniform beam, and (c) single, thickness-variable beam. The von Mises stress (magnitude) and displacement for three deformation states (d)–(f) d_{center} = 0 mm (g)–(i) d_{center} = 3.1 mm and (j)–(l) d_{center} = 5.7 mm for a single beam element in (d), (g), and (j), a double beam element in (e), (h), and (k), and a single beam element with varying thickness in (f), (i), and (l).

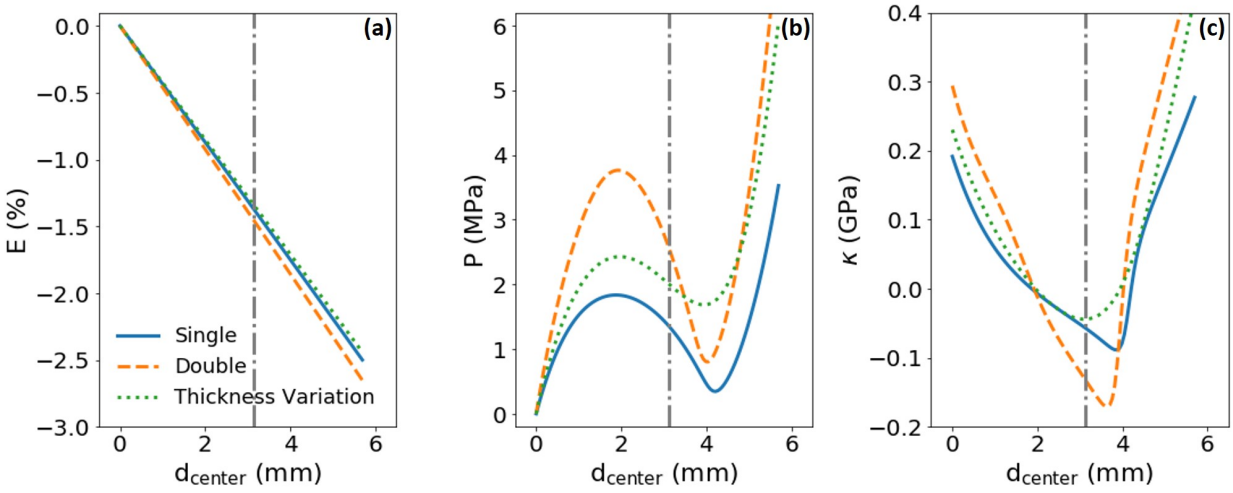

Fig. 7—Comparison of (a) percent strain, (b) pressure in MPa, and (c) incremental stiffness in MPa as a function of the displacement in mm of the center of the outermost beam for three different beam designs: a single beam (solid, blue line), a double beam (dashed, orange line), and a single beam with thickness variation (dotted, green line). Dash-dotted, gray line denotes strain state of deformations.

presented in Fig. 7(c). The magnitude of the negative stiffness for the double-beam inclusion is largest, but the single-beam element is still larger than the beam with variable thickness. Therefore, the use of the thickness variation constrains the structure in such a way that reduces the negative stiffness behavior.

It is also interesting that the displacement states corresponding to the negative stiffness region are identical for all three cases. The relationship between the curvature, thickness, and length of the beam therefore dominates the onset of negative stiffness, since these geometric features were the same in all three cases. This preliminary study indicates that the use of a pressure transformer to limit the applied displacement to the center of the beam is not necessary and could be eliminated to avoid additional fragile features that scale up the inclusion dimensions.

Cylindrical inclusions were fabricated with two single, pre-curved beams of uniform thickness without a pressure transformer arranged perpendicular to one another as pictured in Fig. 8. The length of each beam is 30 mm, with initial apex of 2 mm, thickness of 1 mm, and beam width of 3 mm. The beam structure was fabricated from DigitalABS. An outer layer of TangoPlus was printed on top of the beam structure to create an outer cylinder. Internally, the bottom of the TangoPlus layer is level with the bottom, or inner surface, of the intersecting beams, and follows the beams' curvature.

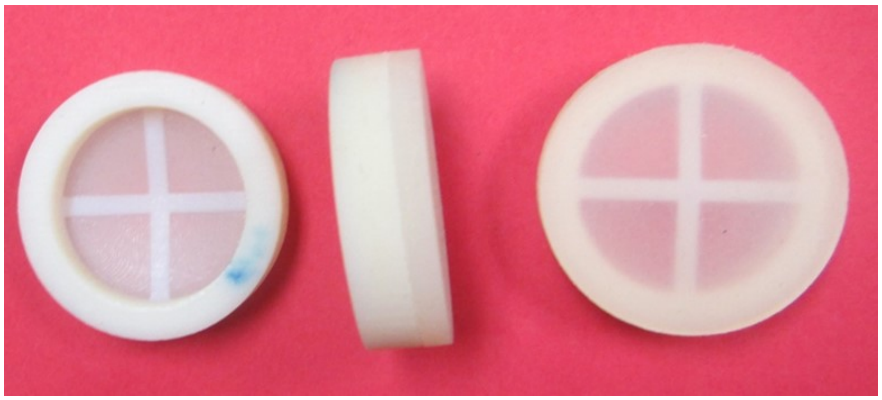

Fig. 8—Halves of cylindrical inclusions designed with the beam element and outer ring fabricated from DigitalABS and a top layer fabricated from TangoPlus

The fabricated inclusion halves were tested with the same ADMET system previously used. However, the compression loading with the ADMET did not deform the inclusions as expected. When a uniform displacement is applied to the surface of the TangoPlus, the elastomer bulges to the sides and does not transfer the loading to the surface of the beam. In order for this design to be tested properly, either the sides of the elastomer must be constrained to deform only in the direction of the uniaxial loading, or the entire element must be under hydrostatic loading. This issue motivates the design of a test apparatus that utilizes hydrostatic loading rather than uniaxial compression. Furthermore, the difficulty in ensuring the matrix does not deform around the beams within the inclusion structure motivates the exploration of a negative stiffness structure that is completely closed cell.

3.4 Pre-curved Plates

A pre-curved plate, rather than pre-curved beam, is one way to achieve a negative stiffness inclusion design that is completely closed-cell. The buckled shape of the pre-curved beam corresponded to the first eigenmode of the clamped-clamped beam. Most designs for buckling structures make use of beam elements. However, designs alternative to a pre-curved beam that still make use of a pressure transformer to displace the center of the unit cell have been explored recently, including cosine-shaped "domes" [42] and truncated conical shells [43]. Both references study the mechanical response of periodic lattices. Though similar in concept, the present design for a pre-curved plate utilizes the first eigenmode of a clamped, circular plate rather than a clamped-clamped beam or membrane. The height of the plate as a function of space is derived here by applying the appropriate boundary conditions to equation of motion of a circular plate, e.g., see Ref. [44], such that

$$H(x) = h\left[\frac{I_0(N_1)\,J_0(N_1 x/a) - J_0(N_1)\,I_0(N_1 x/a)}{I_0(N_1) - J_0(N_1)}\right], \tag{28}$$

where h is the initial apex at the center of the plate, a is the radius of the circular plate, $N_1 = 3.1962$ is the first eigenvalue for a clamped-clamped plate, J_0 is the zeroth order Bessel function of the first kind, and I_0 is the modified zeroth order Bessel function of the first kind.

The same spherical design from Section 3.3 with beam elements is now explored for a thin plate structure. The inclusion design appears in Fig. 9(a), with the front half cut away in Fig. 9(b) to see the internal features. The pre-curved plates have radius $a = 10$ mm, thickness $t = 1$ mm, and initial apex $h = 2$ mm. In Fig. 10,

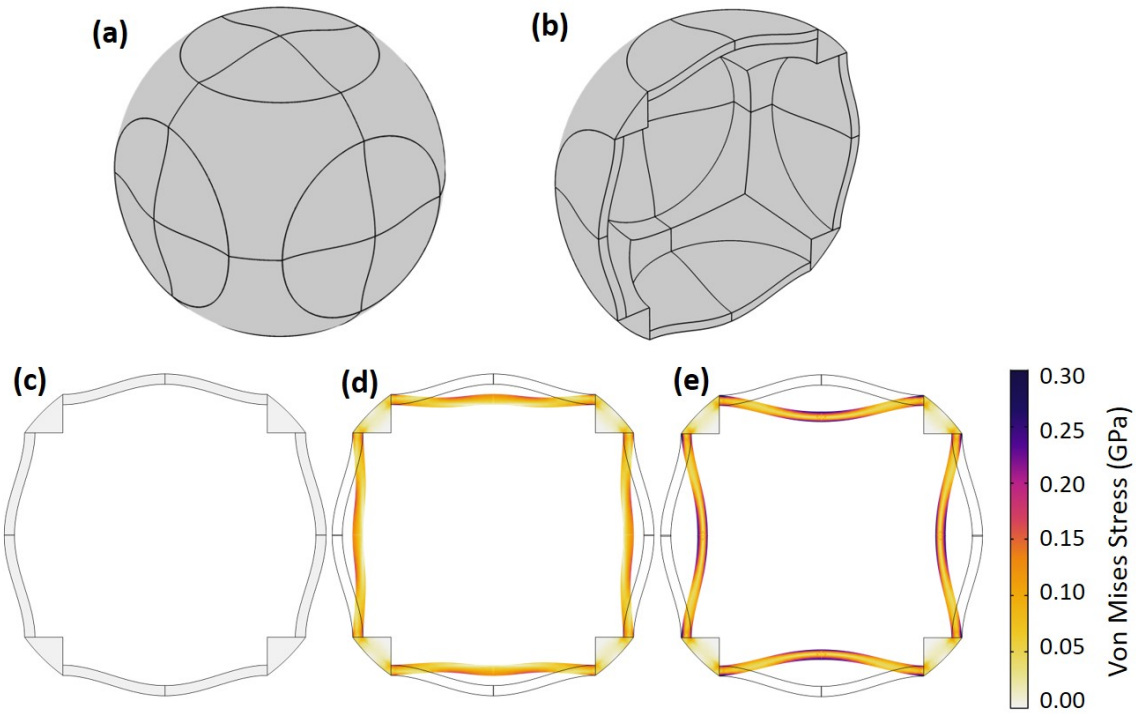

Fig. 9—(a) 3D Inclusion spherical element for pre-curved plates with (b) half the element cut away to show the internal features. Deformation on cut-plane for DigitalABS material at (c) $E = 0\%$ (d) $E = 2.9\%$ and (e) $E = 5.3\%$.

the pressure and stiffness for spherical inclusions with the same geometric design, but different material properties are explored. In Fig. 6(c)–(e), the deformation and von Mises stress along the center cut plane are shown only for one material, DigitalABS. This is because the deformation of the beam is the same regardless of the material. The only difference is in the magnitude of the stress. The displacement of the plate appears similar to that of the single beam. However, unlike the case with a single beam, which could deform into the asymmetric second mode, a uniform circular plate under uniform loading always undergoes axisymmetric deformation [44]. It again is worth noting the increased stress at the center and edges of the plate, which could result in fracture of the structure upon loading.

In considering closed-cell inclusions, the trapped air within the internal cavity becomes important. One example of a closed-cell inclusion is called a "buckliball", in which thin ligaments between holes covered with thin membranes buckle [45]. However, the experiment by Shim et al. evacuates the internal pressure of the sphere and studies the difference between the internal and external pressure. The negative stiffness behavior was not achieved as easily when the inclusions were loaded with an external pressure [46]. Furthermore, Tan et al. compares the response of a single, truncated, conical shell with and without an orifice, and acknowldege a difference in the mechanical properties when air can flow out of the port upon deformation [43]. However, the authors in Ref. [43] provide minimal discussion on the influence the response has on the negative stiffness behavior. This concept is investigated here through numerical simulations.

In Fig. 10, spherical inclusions with the same geometric design, but different material properties, are compared to explore the importance of modeling the air within the internal cavity. In each subfigure, 3 cases are compared: (1) the application of a boundary load on all internal surfaces (solid, blue line), (2) the application of a boundary load on all the external surface (dashed, orange line), and (3) the application of a boundary load on all external surfaces with an internal boundary load on all internal surfaces that represents the pressure of an enclosed air cavity (dotted, green line). In modeling case 3, it is assumed that the air is given by the gas law

$$P = P_0 \left[\left(\frac{V_0}{V} \right)^{1.4} - 1 \right], \tag{29}$$

where P_0 and V_0 are the initial pressure and volume and P and V are the pressure and volume at each

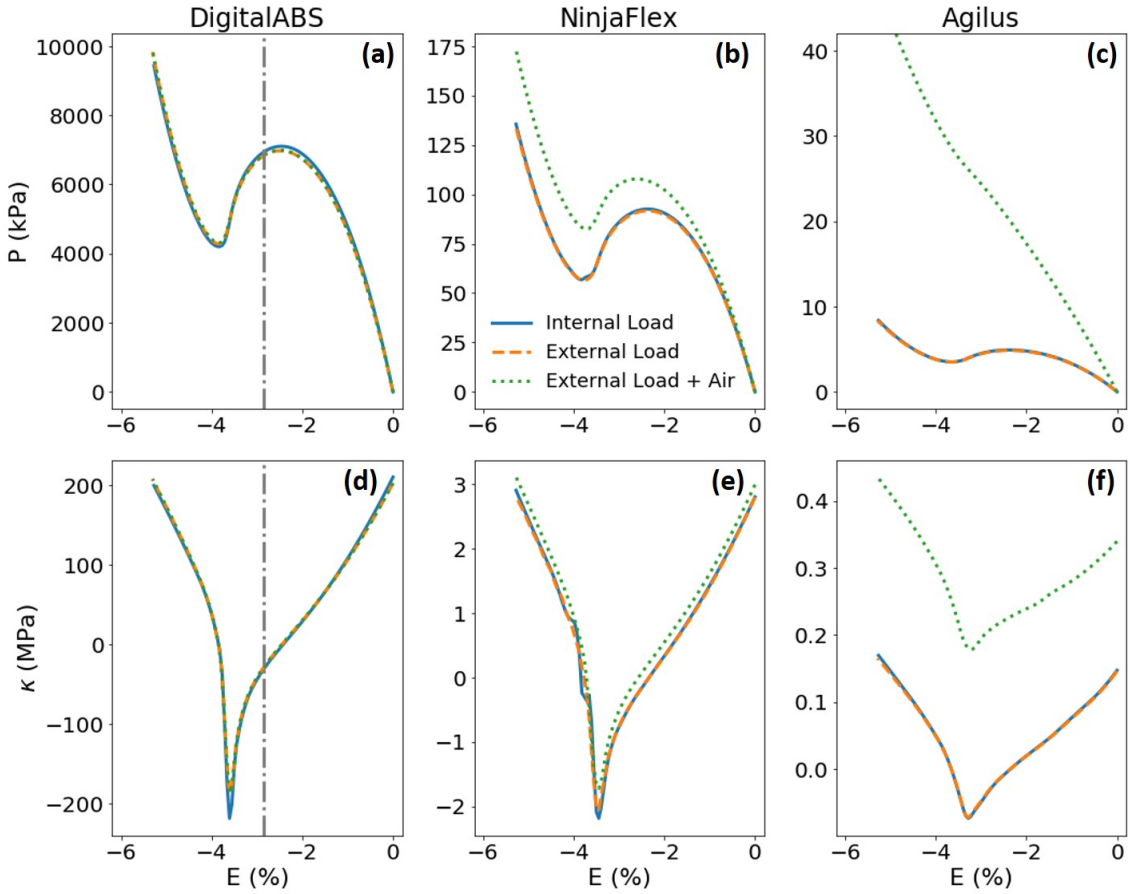

Fig. 10—Comparison of (a)–(c) pressure in MPa and (d)-(f) incremental stiffness in MPa as a function of inclusion strain percent for the same inclusion design with different boundary loads: an internal boundary load only (solid, blue line), an external boundary load only (dotted, orange line), and an external boundary load with an internal pressure load representing the effects of air within an cavity (dotted, green line). Three materials are considered: (a) and (d) DigitalABS, (b) and (e) NinjaFlex, and (c) and (f) Agilus.

deformation state, respectively. The initial pressure P_0 = 1 atm = 101325 Pa. The volume of the air cavity V is obtained in COMSOL by integrating over the internal boundaries of the inclusion S and applying the divergence theorem, such that

$$V = \int_V \mathrm{d}V = \int_V \nabla \left(x e_{xx} + y e_{yy} + z e_{zz} \right) \mathrm{d}V = -\frac{1}{3} \int_S \left(x n_x + y n_y + z n_z \right) \mathrm{d}S. \tag{30}$$

Note that the negative sign is due to the direction of the normal n_i in COMSOL.

In Figs. 10(a) and 10(d), a linear elastic model for DigitalABS with material properties from Table 1 are utilized. All three cases are nearly identical for the pressure in 10(a) and stiffness in 10(d). In Fig. 10(b) and 10(e), a Murnaghan hyperelastic model is used for NinjaFlex with material properties from Table 2. The case of internal loading and external loading in the absence of air within the cavity are once again nearly the same, as shown in Fig. 10(b). However, there is an increase in pressure as a function of deformation when the air is accounted for. The trend for the case with an external load while accounting for the internal pressure is similar to the two cases without the internal air, but indicates an increase in pressure required to achieve the same deformation. The effect on the incremental stiffness is minimal, as illustrated in Fig. 10(e). The pressure is increased further for a softer material, which is evident in Fig. 10(c) and 10(f), where a Murnaghan model for Agilus based on Table 2 is employed. The cases of the internal load only and the external load only are again nearly the same, but the case of the external load while accounting for the internal pressure due to the air cavity is very different in Fig. 10(c). The curve for the external load with air is now monotonic and corresponds to a deformation with no negative stiffness. This is illustrated explicitly in Fig. 10(f) by the purely positive stiffness curve shown in the dotted, green line.

It is therefore possible to constrain a closed-cell, negative stiffness inclusion purely by the air encapsulated within the structure. This would occur for any case in which the required pressure load to achieve the desired deformation is on the order of or less than that of the pressure within the cavity. In this study, the same inclusion design modeled with different materials demonstrated the influence of the effective pressure due to the medium contained within the closed cavity. However, changes in geometric features of the inclusion, e.g., initial curvature or radius of the plate, also will alter the magnitude of the external pressure loading. Therefore, the influence of the changing internal pressure within the cavity is critical to designing inclusions to behave as expected and need to be accounted for properly. This adds an additional difficulty in designing closed-cell inclusions for acoustic applications. Note that this is also important for the case of beam elements studied in Section 3.3. When encapsulated in a matrix material, there will be an internal cavity enclosed with air unless evacuated upon assembly. This study indicates that while using the eigenmode of a plate is applicable to the design of a negative stiffness inclusion, closed-cell structures must be considered carefully to ensure the desired negative stiffness actually will be present.

This study also, as anticipated, demonstrated that the case of applying a positive external load to the outer boundary is the same as applying a negative load to the internal boundary. Therefore, an experiment to verify the pressure-strain response could be performed by evacuating the air within the structure, rather than sealing the inclusion within a pressure chamber to apply an external load. Of course, for inclusions with low overall stiffness, the pressure due to the air within the changing volume of the cavity still may constrain the inclusion to eliminate the negative stiffness effect.

Samples with pre-curved plates were fabricated into cylindrical inclusions as shown in Fig. 11 using a Stratasys J750 Polyjet printer. Each inclusion has an overall diameter of 29 mm and includes two pre-curved

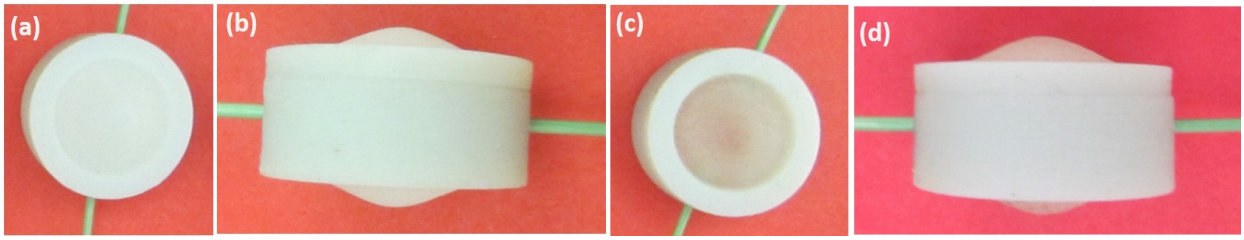

Fig. 11—An inclusion with an outer shell fabricated in two parts from Digital ABS with a pre-curved plate made of (a) DigitalABS, viewed from the top, (b) DigitialABS, viewed from the side, (c) TangoPlus, viewed from the top, and (d) TangoPlus, viewed from the side

plates, each with a 10 mm radius, thickness of 1 mm, and an initial apex equal to 2 mm. Two small ports were fabricated within the inclusion, one with tubing connect to a vacuum pump to evacuate internal pressure, and another to be able to measure the current internal pressure. In Fig. 11, (a) a top view and (b) a side view are shown for a plate fabricated entirely from DigitalABS. The plate appears perfectly symmetric. An inclusion with the same geometric features as in Fig. 11(a)–(b) is shown in Fig. 11(c)–(d) for different material properties. For this inclusion, the plates are fabricated from Agilus, while the outer ring is fabricated from DigitalABS, with the top view in Fig. 11(c) and the side view in Fig. 11(d). In part Fig. 11(d), the inclusion no longer appears symmetric due to the imperfect recovery from an imposed deformation.

Both plates were tested by evacuating the internal structure. The inclusion fabricated only from DigitalABS required a much higher pressure to evacuate the plates. However, snap-through was observed as the plate reached a point of instability. For the inclusion fabricated from both DigitialABS and Agilus, a much lower pressure was required and the inclusion did not appear to snap through. The analysis above indicates that the multi-material inclusion is too soft to achieve the desired negative stiffness. However, this test proved that multi-material designs are viable. As discussed in Section 2.2, Stratasys offers the ability to fabricate digital materials, where a combination of DigitialABS and Agilus could be combined to form a material with intermediate stiffness. The outer ring should be approximately rigid and thus fabricated from a stiffer plastic. Further testing is required to fully explore the capabilities of negative stiffness inclusions fabricated from digital materials.

4. COMPOSITE MATERIALS

Of interest with respect to the design of the inclusions with negative stiffness is its effect on the overall deformation of a composite material. Here, a COMSOL model is used to obtain the pressure-strain response for one inclusion embedded in a hyperelastic matrix material. One-eighth of the composite is directly modeled due to symmetry conditions. Only one inclusion is considered here to exemplify the composite behavior: a spherical inclusion containing pre-curved plates with $a = 10$ mm, thickness $t = 1$ mm, and initial height $h = 2$ mm made entirely from DigitalABS, as discussed in Section 3.4. The inclusion is embedded in a spherical matrix with $K_M = 2$ GPa, and a varying shear modulus. For simplicity, the matrix is modeled using a nearly incompressible Neo-Hookean model. By volume, the inclusion is only 1% of the overall composite. A pressure boundary load is applied to the outer surface of the matrix sphere and the volume change of both the inclusion and the matrix material are obtained as a function of deformation.

In Fig. 12(a), the pressure boundary load in MPa is presented as a function of inclusion strain for four cases: the composite with $G_M = 0.01$ MPa (blue curve), the composite with $G_M = 1$ MPa (orange curve),

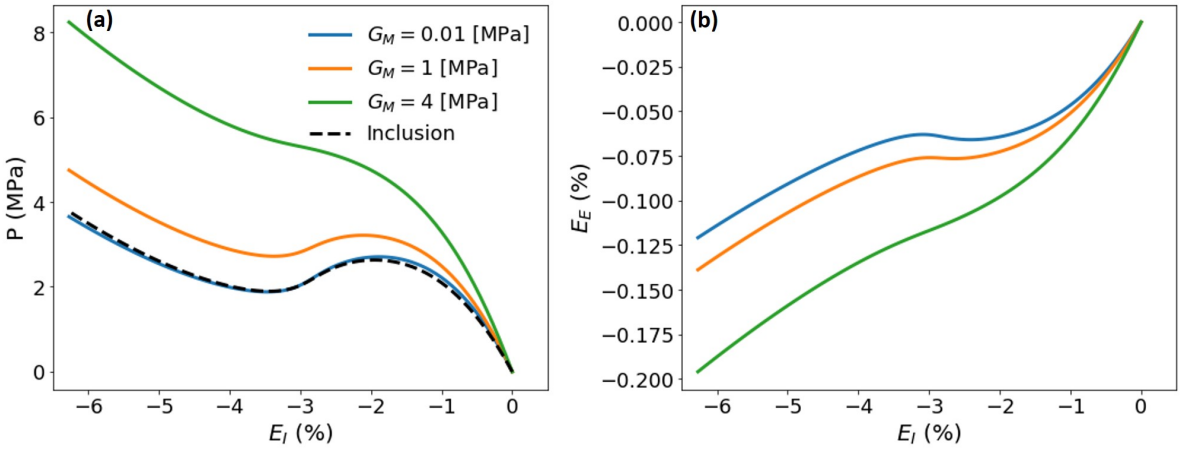

Fig. 12—(a) Pressure loading in MPa and (b) effective medium strain percent as a function of inclusion strain percent for a composite media containing 1% negative stiffness inclusion within a nearly incompressible, Neo-Hookean matrix with K_M = 2 GPa and G_M = 0.01 MPa (blue line), G_M = 1 MPa (orange line), and G_M = 4 MPa (green line). The black, dashed line corresponds to the response of the inclusion.

the composite with G_M = 4 MPa (green curve), and the inclusion only with no matrix (black, dashed curve). The composite with G_M = 0.01 MPa represents a case in which the matrix is very soft, and the overall pressure-strain response is similar to that of just the inclusion. In the case of a fluid, heterogeneous media undergo iso-stress loading such that the pressure is the same everywhere. Thus, it is anticipated that if the matrix shear modulus is too low, it would behave similarly to a fluid. This corresponds to a composite material with deformation states representing macroscopic instabilities, or macroscale negative stiffness. As the shear modulus is increased, the magnitude of the pressure also increases, as evident by the composite case for G_M = 1 MPa. However, this matrix is still too soft to fully constrain the inclusion within the negative stiffness regime. Further increasing the shear modulus, such as to G_{M} = 4 MPa, creates a composite that is stable for every strain state and can constrain the inclusion within its negative stiffness regime.

The inclusion deformation is the same for each case of the composite material considered. Therefore, the inclusion strain is the same. However, the effective medium strain is not, as illustrated in Fig. 12(b) for G_M = 0.01 MPa (blue curve), the composite with G_M = 1 MPa (orange curve), and the composite with G_M = 4 MPa (green curve). The strain on the inclusion scale is an order of magnitude larger than the effective medium, indicating that the change in volume is much smaller for the effective composite material than the inclusion. Therefore, the large deformation is localized to the surface of the negative stiffness inclusion, limiting the overall volume change even at higher pressures.

The incremental stiffness as a function of inclusion strain percent appears in Fig. 13(a) for one inclusion K_M = 2 GPa, and the composite with 13(b) G_M = 0.1 MPa, 13(c) G_M = 1 MPa, and 13(d) G_M = 4 MPa. The overall trends are the same, with local minima appearing in all cases near E_I = 3%. For the inclusion in Fig. 13(a), the stiffness is on the order of tens of MPa, and becomes negative for some strain states. Negative stiffness also occurs for the effective κ of the composite at G_M = 0.01 MPa in Fig. 13(b) and G_{M} = 1 MPa in Fig. 13(c), but is two orders of magnitude larger than the inclusion, on the order of GPa. The negative stiffness regime for G_M = 1 MPa is reduced in both magnitude and amount of corresponding strain states

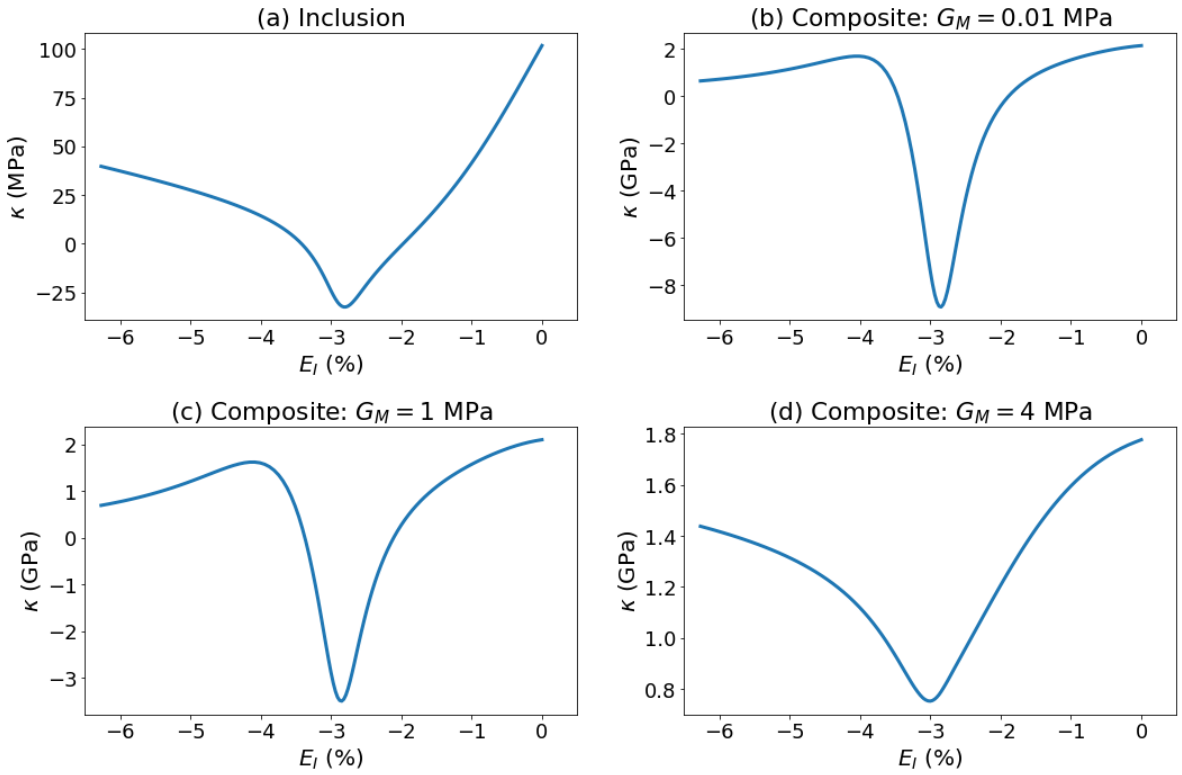

Fig. 13—Incremental stiffness as a function of inclusion strain percent for (a) one inclusion only, and a composite media containing 1% negative stiffness inclusion within a nearly incompressible, Neo-Hookean matrix with K_M = 2 GPa and (b) G_M = 0.1 MPa, (c) G_M = 1 MPa, and (d) G_M = 4 MPa

relative to G_M = 0.01 MPa, indicating that the matrix is beginning to constrain the negative stiffness of the inclusion. For the case in which G_M = 4 MPa in Fig. 13(d), the stiffness is fully positive and indicates a much smaller variation in κ as a function of strain. However, the effective stiffness still should yield a favorable acoustic response.

In an effort to fabricate a composite structure, one test cylinder fabricated entirely from DigitalABS, as discussed in Section 3.4, was embedded within PDMS as shown in Fig. 14. A small mold was fabricated and was filled halfway with uncured PDMS. The inclusion then was placed within the half of uncured PDMS such that it was half submerged. When air-filled, the inclusion is positively buoyant compared to the uncured elastomer, meaning it will shift upwards rather than sink. The PDMS was left overnight to cure fully. By partially submerging the inclusion, it attaches to the PDMS when cured. Once the first half was cured fully, the remainder of the mold was filled with uncured PDMS and again was left overnight to cure fully. Because the uncured polymers were the same ratios of components, the line dividing the two halves of the PDMS is indistinguishable in Fig. 14(a). This test fabrication provides a method to fabricate such a composite medium that could be tested under either mechanical or acoustic loading.

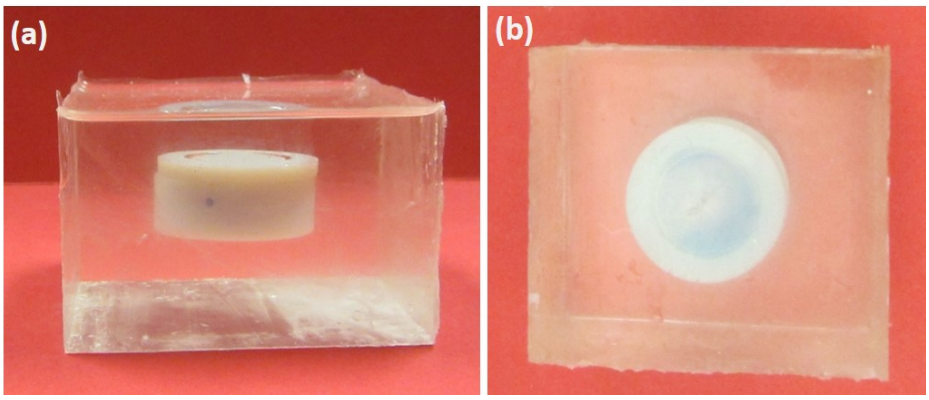

Fig. 14—The (a) side view and (b) top view of an inclusion with pre-curved plates printed from DigitalABS embedded in PDMS

5. CONCLUSION

This work considers the design, modeling, and fabrication of structures containing negative stiffness inclusions for application to underwater acoustics. The trade-off between the scale of the inclusion and the operation frequencies of interest motivates the exploration of small structures with potentially fragile components. Such thin features are more difficult to fabricate and more susceptible to failure, as evident through initial testing of structures with a pressure transformer that localized the displacement. This motivated the consideration of alternative designs. Two viable designs were explored with numerical studies and preliminary testing. The first is an inclusion with pre-curved beam elements that eliminates a pressure transformer to undego uniform pressure loading. The second is an inclusion with pre-curved plates underoging uniform pressure loading. Numerical studies on the effective medium response of a composite with a low volume fraction of such inclusions were performed to further illustrate the change in response with the host matrix.

Also demonstrated in this work is the importance of the back-filled material within the internal cavity closed-cell structure. Often, the effective pressure of the internal cavity with encapsulated negative stiffness inclusions is neglected. However, in analyzing the closed-cell design containing pre-curved beams, it was determined that the incident pressure of the internal boundaries is just as important as the effective pressure on the outer boundaries of the inclusion. This internal pressure has a profound effect on the overall deformation when it is the same order of magnitude as the required pressure load, resulting in constrained negative stiffness even though the inclusion is not embedded in a sufficiently stiff host material. Therefore, the influence of the physical and geometric properties is even more critical in designing a closed-cell negative stiffness inclusion.

The present analyses offer a path toward addressing the trade-off in tolerance to hydrostatic pressure loadings with optimal acoustic performance through studying structures that achieve negative stiffness while eliminating the often-used pressure transformer, which can be very fragile and susceptible to fracture. Future work should focus on optimization of designs to achieve the intended acoustic response, including use of multiple inclusions with varying activation to achieve a more broadband response. Experimental verification of such behavior also should follow.

ACKNOWLEDGMENTS

This work was funded by The Jerome and Isabella Karle Distinguished Scholar Fellowship Program.

REFERENCES

1. P. Meresse, C. Audoly, C. Corenne, and A. C. Hladky-Hennion, "Acoustic coatings for maritime systems applications using resonant phenomena," *Comptes Rendus Mecanique* **343**(12), 645–655 (2015).
2. Y. C. Wang and R. S. Lakes, "Extreme thermal expansion, piezoelectricity, and other coupled field properties in composites with a negative stiffness phase," *J. Appl. Phys* **90**(12), 6458–6465 (2001).
3. R. S. Lakes, T. Lee, A. Bersie, and Y. C. Wang, "Extreme damping in composite materials with negative-stiffness inclusions," *Nature* **410**, 565–567 (2001).
4. R. S. Lakes, "Extreme damping in composite materials with a negative stiffness phase," *Phys. Rev. Lett.* **86**(13), 2897–2900 (2001).
5. R. S. Lakes, "Extreme damping in compliant composites with a negative-stiffness phase," *Phil. Mag. Lett.* **81**(2), 95–100 (2001).
6. R. S. Lakes and W. J. Drugan, "Dramatically stiffer elastic composite material due to a negative stiffness phase?," *J. Mech. Phys. Solids* **50**, 979–1009 (2002).
7. Y. C. Wang, M. Ludwigson, and R. S. Lakes, "Deformation of extreme viscoelastic metals and composites," *Mat. Sci. Eng. A-Struct.* **370**, 41–49 (2004).
8. Y. C. Wang and R. S. Lakes, "Extreme stiffness systems due to negative stiffness elements," *Am. J. Phys.* **72**(1), 40–50 (2004).
9. T. Jaglinski, D. Kochmann, D. Stone, and R. S. Lakes, "Composite materials with viscoelastic stiffness greater than diamond," *Science* **315**, 620–622 (2007).
10. C. S. Wojnar and D. M. Kochmann, "A negative-stiffness phase in elastic composites can produce stable extreme effective dynamics but not static stiffness," *Philos. Mag.* **94**(6), 532–555 (2013).
11. D. M. Kochmann and K. Bertoldi, "Exploiting microstructural instabilities in solids and structures: From metamaterials to structural transitions," *Appl. Mech. Rev.* **69**, 050801 (2017).
12. M. R. Haberman and M. D. Guild, "Acoustic Metamaterials," *Physics Today* **69**(6), 43–48 (2016).
13. N. Nadkarni, C. Daraio, and D. M. Kochmann, "Dynamics of periodic mechanical structures containing bistable elastic elements: From elastic to solitary wave propagation," *Phys. Rev. E* **90**, 023204 (2014).
14. Z. Wu, R. L. Harne, and K. W. Wang, "Exploring a modular adaptive metastructure concept inspired by muscle's cross-bridge," *J. Intell. Mater. Syst. Struct.* (2015).
15. L. Dong and R. Lakes, "Advanced damper with high stiffness and high hysteresis damping based on negative strucutral stiffness," *Int. J. Solids Struc.* **50**, 2416–2423 (2013).
16. H. Kalathur and R. S. Lakes, "Column dampers with negative stiffness: high damping at small amplitudes," *Smart Mater. Struc.* **22**, 084013 (2013).

17. T. Klatt and M. R. Haberman, "A nonlinear negative stiffness metamaterial unit cell and small-on-large multiscale material model," *J. Appl. Phys.* **114**, 033503 (2013).

18. S. Cortes, J. Allison, C. Morris, M. R. Haberman, C. Seepersad, and D. Kovar, "Design, manufacture, and quasi-static testing of metallic negative stiffness structures within a polymer matrix," *Exp. Mech.* **57**, 1183–1191 (2017).

19. D. M. Correa, T. Klatt, S. Cortes, M. Haberman, D. Kovar, and C. Seepersad, "Negative stiffness honeycombs for recoverable shock isolation," *Rapid Prototyping J.* **21**(2), 193–200 (2015).

20. D. Chronopoulos, I. Antoniadis, and T. Ampazidis, "Enhanced acoustic insulation properties of composite metamaterials having embedded negative stiffness inclusion," *Extreme Mech. Lett.* **12**, 48–54 (2017).

21. K. Alur and J. Meaud, "Nonlinear mechanics of non-dilute viscoelastic layered composites," *Int. J. Solids and Struct.* **72**, 130–143 (2015).

22. T. Sain, J. Meaud, G. Hulburt, E. M. Arruda, and A. M. Waas, "Simultaneously high stiffness and damping in a class of wavy layered composites," *Adv. Mater.* **27**, 4296–4301 (2013).

23. D. D. Quinn, S. Hubbard, N. Wierschem, M. A. Al-Shudeifat, R. J. Ott, J. Luo, B. F. Spencer Jr., D. M. McFarland, A. F. Vakakis, and L. A. Bergman, "Equivalent modal damping, stiffening and energy exchanges in multi-degree-of-freedom systems with strongly nonlinear attachments," *J. Multi-body Dynamics* **226**(2), 122–146 (2012).

24. M. A. Al-Shudeifat, "Highly efficient nonlinear energy sink," *Nonlinear Dyn.* **76**, 1905–1920 (2014).

25. J. Bishop and R. L. Harne, "Leveraging the arrangement of multiple, critically constrained inclusions in resonant metamaterials for control of broadband vibroacoustic energy," *Appl. Acoust.* **130**, 222–229 (2018).

26. S. G. Konarski, M. R. Haberman, and M. F. Hamilton, "Frequency-dependent behavior of media containing pre-strained nonlinear inclusions: Application to nonlinear acoustic metamaterials," *J. Acoust. Soc. Am.* **144**(5), 3022–3035 (2018).

27. S. G. Konarski, M. R. Haberman, and M. F. Hamilton, "Acoustic response for nonlinear, coupled multiscale model containing subwavelength designed microstructure instabilities," *Phys. Rev. E* **101**, 022215 (2020).

28. C. Morris, L. Bekker, C. Spadaccini, M. Haberman, and C. Seepersad, "Tunable mechanical metamaterial with constrained negative stiffness for improved quasi-static and dynamic energy dissipation," *Adv. Eng. Mater.* **21**(7), 1900163 (2019).

29. B. M. Goldsberry, S. P. Wallen, and M. R. Haberman, "Non-reciprocal wave propagation in mechanically-modulated continuous elastic metamaterials," *J. Acoust. Soc. Am.* **146**(1), 782–788 (2019).

30. Z. Wu, Y. Zheng, and K. W. Wang, "Metastable modular metastructure for on-demand reconfiguration of band structures and nonreciprocal wave propagation," *Phys. Rev. E* **97**(2), 022209 (2018).

31. K. Bertoldi and M. C. Boyce, "Wave propagation and instabilities in monolithic and periodically structured elastomeric materials undergoing large deformations," *Phys. Rev. B* **78**, 184107 (2008).

32. P. Wang, F. Casadei, S. Shan, J. C. Weaver, and K. Bertoldi, "Harnessing buckling to design tunable locally resonant acoustic metamaterials," *Phys. Rev. Lett.* **113**, 014301 (2014).

33. J. Qiu, J. H. Lang, and A. H. Slocum, "A curved-beam bistable mechanism," *J. Microelectromech. S.* **13**(2), 137–146 (2004).

34. M. F. Hamilton, Yu. A. Ilinskii, and E. A. Zabolotskaya, "Separation of compressibility and shear deformation in the elastic energy density (L)," *J. Acoust. Soc. Am.* **116**(1), 41–44 (2004).

35. ASTM Standard 638-02a, *Standard test method for tensile properties of plastics* (ASTM International, West Conshokocken, PA, 2002).

36. S. M. Ross, *Introduction to Probability and Statistics for Engineers and Scientists*, pp. 180–182, 223–231, 348–349, 572 (Academic Press, 2nd ed., 2000).

37. ASTM Standard 412-06a, *Standard test method for vulcanized rubber and thermoplastic elsatomers - Tension* (ASTM International, West Conshokocken, PA, 2006).

38. P. Virtanen, R. Gommers, T. E. Oliphant, M. Haberland, T. Reddy, D. Cournapeau, E. Burovski, P. Peterson, W. Weckesser, J. Bright, S. J. van der Walt, M. Brett, J. Wilson, K. Jarrod Millman, N. Mayorov, A. R. J. Nelson, E. Jones, R. Kern, E. Larson, C. Carey, İ. Polat, Y. Feng, E. W. Moore, J. Vand erPlas, D. Laxalde, J. Perktold, R. Cimrman, I. Henriksen, E. A. Quintero, C. R. Harris, A. M. Archibald, A. H. Ribeiro, F. Pedregosa, P. van Mulbregt, and Contributors, SciPy 1. 0, "SciPy 1.0: Fundamental Algorithms for Scientific Computing in Python," *Nature Methods* (2020), doi:https://doi.org/10.1038/s41592-019-0686-2.

39. V. Slesarenko and S. Rudykh, "Towards mechanical characterization of soft digital materials for multimaterial 3D printing," *Int. J. Eng. Sci.* **123**, 62–72 (2018).

40. M. Sasso, G. Palmieri, G. Chiappini, and D. Amodio, "Characterization of hyperelastic rubber-like materials by biaxial and uniaxial stretching tests based on optical methods," *Polym. Test* **27**, 995–1004 (2008).

41. S. G. Konarski, *Tunable, nonlinear acoustic metamaterials due to subwavelength structural instabilities*, PhD thesis (The University of Texas at Austin, 2017).

42. M. Alturki and R. Burgueño, "Response characterization of multistable shallow domes with cosine-curved profile," *Thin Wall. Struct.* **140**, 74–84 (2019).

43. X. Tan, B. Wang, S. Zhu, S. Chen, K. Yao, P. Xu, L. Wu, and Y. Sun, "Novel multidirectional negative stiffness mechanical metamaterials," *Smart Mater. Struct.* **29**, 015037 (2019).

44. A. W. Leissa, *Vibration of Plates*, pp. 7–8 (Scientific and Technical Information Division, National Aeronautics and Space Administration, 1969).

45. J. Shim, C. Perdigou, K. R. Chen, K. Bertoldi, and P. M. Reis, "Buckling-indcued encapsulation of structured elastic shells under pressure," *P. Natl. Acad. Sci. USA* **109**(16), 5978–5983 (2012).

46. S. G. Konarski, M. R. Haberman, P. S. Wilson, K. Bertoldi, S. Babaee, and J. Shim, "Experimental determination of pressure-dependent stiffness of a nonlinear acoustic metamaterial," *J. Acoust. Soc. Am.* **139**(4), 2183–2183 (2016).